Acoustic emission based health monitoring of RC corroded beams strengthened by CFRP anchorage system under bending loads

Pan, Tanbo; Shu, Zijun; Liu, Yongcheng; Aydin, Beyazit Bestami; Li, Yang; Zhou, Yujue; Zhou, Yubao

DOI
10.1016/j.compstruct.2025.119514

Publication date
2025

Document Version
Final published version

Published in
Composite Structures

Composite Structures 372 (2025) 119514

Contents lists available at ScienceDirect

Composite Structures

journal homepage: www.elsevier.com/locate/compstruct

Acoustic emission based health monitoring of RC corroded beams strengthened by CFRP anchorage system under bending loads

Tanbo Pan [a,b], Zijun Shu [a], Yongcheng Liu [b,*], Beyazit Bestami Aydin [c], Yang Li [d], Yujue Zhou [b], Yubao Zhou [e]

[a] School Civil Engineering & Architecture, East China Jiaotong University, China
[b] Department of Hydraulic Engineering, Civil Engineering college, Tongji University, China
[c] Department of Civil Engineering, Middle East Technical University (METU), Turkey
[d] Kunming Institute of Physics, China
[e] Faculty of Civil Engineering and Geosciences, Delft University of Technology, Netherlands

ARTICLE INFO

Keywords:
Acoustic emission
CFRP anchorage system
Corroded beams
Damage mechanism
Structure monitoring

ABSTRACT

This study explores the damage evolution and crack behavior exhibited by CFRP-strengthened corroded RC beams subjected to bending loads, with the application of AE monitoring. The results show that three primary failure modes were observed: concrete cover separation, debonding of the CFRP sheet with anchor pullout and matrix cracking and fiber tearing, with the middle mode exhibiting greater ductility. AE ringing counts analysis effectively divided the damage process into three stages: initial damage, damage development, and continuous damage. Signal intensity analyses provided insights into damage severity, revealing enhanced crack propagation in corroded beams, while severe corrosion reduced AE signal frequency and intensity in later stages, indicating initial crack activity inhibition and accelerated damage in mild to moderate corrosion. The Ib-value demonstrated trends in ductility and damage severity, with higher ductility in less corroded beams and restricted damage development in heavily corroded ones. RA-AF crack classification and Gaussian Mixture Clustering identified an increased proportion of shear cracks with higher corrosion levels, reducing shear load-carrying capacity. These findings highlight AE-based monitoring as an effective tool for real-time damage assessment in CFRP-strengthened RC beams.

1. Introduction

Corrosion of steel reinforcement within reinforced concrete (RC) structures is a pervasive issue that significantly compromises the structural integrity and durability of civil infrastructure globally. The degradation process reduces the cross-sectional area of steel bars and impairs their mechanical properties, such as strength and ductility. Moreover, corrosion undermines the bond between steel bars and concrete, which is crucial for load transfer within RC structures. The cumulative effect of these changes poses substantial risks to both the safety and functional longevity of such constructions, as documented in several studies [1–5].

In response to these challenges, the use of Fiber Reinforced Polymer (FRP) composites has been increasingly adopted as a strengthening solution in civil engineering due to its superior mechanical properties. FRP materials are celebrated for their high strength-to-weight ratio, exceptional corrosion resistance, enhanced fatigue resistance, and long-term durability. Additionally, FRP can be easily fabricated and installed, making it an attractive option for reinforcing aging infrastructure [6–10]. However, integrating FRP with existing concrete structures presents unique challenges, particularly the risk of premature debonding. FRP sheets may detach from the concrete substrate before they have effectively mobilized their full tensile strength due to insufficient bonding [11–13]. To address the problem of debonding, specialized FRP anchorage systems have been developed. These systems are designed to improve the adhesion between FRP materials and concrete surfaces significantly. By effectively managing the stresses that occur particularly at the ends of the FRP sheets—where longitudinal and transverse peel stresses are most intense—these anchorage systems help prevent or delay the onset of debonding at the FRP termination zones [14–16].

Despite these advancements, FRP-strengthened concrete structures are not without limitations. The nature of FRP composites, characterized

* Corresponding author at: Department of Hydraulic Engineering, Civil Engineering college, Tongji University, China.
E-mail addresses: yongcheng.liu@kuleuven.be (Y. Liu), beyazit@metu.edu.tr (B.B. Aydin).

https://doi.org/10.1016/j.compstruct.2025.119514
Received 6 February 2025; Received in revised form 11 June 2025; Accepted 24 July 2025
Available online 25 July 2025

by significant elastic deformation and relatively minimal plastic deformation, can lead to abrupt failures in cases of localized damage or when the FRP itself is compromised. The interaction between FRP and concrete under load introduces complex interfacial damage mechanisms, making the failure modes under operational conditions intricate and challenging to predict [17–19]. Given the complexity of these interactions, conventional mechanical analysis often falls short in providing accurate diagnostics or effective damage evaluations. Unlike prior studies focusing on uncorroded beams or conventional CFRP strengthening, this work integrates AE monitoring with a CFRP anchorage system for corroded RC beams, establishing novel corrosion-dependent damage evolution patterns. Methodologically, we enhance Ib-value analysis and Gaussian Mixture Clustering to quantify shear-tensile crack transitions under corrosion, offering new insights for real-time structural health monitoring.

Acoustic Emission (AE) technology is a cutting-edge and practical non-destructive testing approach that has experienced rapid advancements in recent years [20–23]. Its underlying principle involves deploying AE sensors to capture AE signals generated during the deformation and cracking of structures. These signals are then analyzed by an AE system to extract characteristic parameters and waveforms that offer insights into the material's damage evolution. Compared to other non-destructive monitoring methods, AE technology offers several notable advantages, including long-term real-time monitoring, high sensitivity to minimal damage, non-interference with equipment operation, and the absence of external energy input requirements. Consequently, AE techniques have found widespread use across diverse engineering domains, encompassing applications in metal, semi-rigid substrates, grouting sleeves, masonry structures, concrete structures, and more [24–27].

The analysis methods of AE signals can be divided into two categories: AE parameter analysis and AE waveform analysis [21,28,29]. AE parameters include AE hits, duration, ringing count, peak frequency, amplitude and energy, all of which can reflect the crack activities and the structural damage. AE waveform analysis includes spectrum analysis, short Fourier transform, Hilbert-Huang transform, and spectral kurtosis [30,31]. Since AE waveform analysis utilizes full signal information, processing and interpreting AE waveforms can be time-intensive when signal volumes are large. Therefore, compared to AE waveform analysis, AE parameter analysis is widely used because of its efficiency, practicality and simplicity. Ohtsu et al. [32,33] introduced the AE rate theory to evaluate the acoustic emission activity and proposed an empirical formula between acoustic emission parameters and stress levels. Yun et al. [34] investigated the damage evolution of CFRP-strengthened RC beams under three-point bending and created a user-friendly health monitoring system. The results found that the signal characteristics, including event, amplitude versus frequency, and amplitude versus duration, showed apparent differences in the different loading stages, representing other damage mechanisms. Variations in b-values can be used to study crack processes, as elastic waves generated by brittle material damage resemble seismic waves. Sagar et al. [35] investigated the fracture processes of RC beams with loading rate using AE techniques. The results confirmed that when the loading rate is higher, quick cracking development leads to rapid fluctuations and drops in the b-values. Ma et al. [36] revealed that the variation of b-values could effectively reflect the crack development of FRP-strengthened during the cyclic test. Besides, AE intensity analysis is used to assess structural integrity and load-bearing capacity degradation level by tracking two indices,i.e., Historic Index (*HI*) and Severity Index (*SI*). Li et al. [37] applied AE intensity analysis to assess the damage levels of the corroded and uncorroded PVA fibre concrete specimens. El Batanouny et al. [38] and Di et al. [39] determined crack movements and classified damage levels of prestressed reinforced concrete and RC slab structures in accordance with AE intensity analysis.

This study aims to investigate the damage evolution mechanism of corroded RC beams with a CFRP anchorage system under a four-point bending test using AE monitoring. To conduct the investigation, four RC beams were subjected to accelerated electrochemical corrosion to induce varying corrosion levels. Subsequently, all specimens were reinforced with the CFRP anchorage system and subjected to flexural testing until failure. AE sensors were strategically placed to collect signals generated during the loading process, enabling the analysis of crack initiation and damage evolution in the CFRP-strengthened corroded beams. The analysis included AE characteristic parameter analysis, intensity analysis, b-value analysis, and RA-AF crack classification to gain insights into the condition of crack generation and damage development in the specimens.

2. Experimental setup

2.1. Materials and specimens

Four reinforced concrete beams were fabricated with dimensions of 150 mm × 200 mm × 1600 mm. The concrete mixture followed a design ratio of 1:1.65:2.52 (cement: sand: aggregate proportions by volume), and the water-to-cement ratio (w/c) was 0.47 (water: cement proportion by weight). Fig. 1 illustrates the reinforcement details. For enhancing the structural strength, two Φ14-HRB400 steel bars, each with a length of 1800 mm, were positioned at the bottom of the beams to serve as tensile bars. At the top of the beams, two Φ8-HRB400 steel bars, totaling 1600 mm in length, were used as erection bars. The stirrups, made from Φ6-HRB400 steel bars, were evenly spaced from the beam's end at 80 mm intervals. To mitigate stirrup corrosion, epoxy resin was applied at the contact point between the stirrups and longitudinal tensile bars. Additionally, a 25 mm concrete cover was provided to further protect the reinforcement.

Table 1 presents the mechanical properties of the steel bars, concrete, and CFRP sheets utilized in the study. The concrete beam exhibited a compressive strength of 42.5 MPa, with a standard deviation of 3.6 MPa, ensuring its structural stability. The yield strengths of the longitudinal bars in the lower and upper regions were 462.2 MPa and 408.9 MPa, respectively, with standard deviations of 15.2 MPa and 5.5 MPa. Their ultimate strengths were recorded as 615.7 MPa and 611.3 MPa, respectively, with standard deviations of 16.2 MPa and 4.5 MPa. The elastic modulus for both regions was 200 GPa. As for the CFRP sheet, it had a thickness of 1.02 mm, a tensile strength of 3000 MPa, an elastic modulus of 230 GPa, and an ultimate strain of 1.66 %. These material properties were provided by the manufacturer.

2.2. Accelerated steel corrosion process

The concrete specimens were placed on the corrosion trough with the exposed tensile bars outside the trough, which could effectively prevent corroded fracture of tensile bars form moisture, oxygen and chloride ions in the trough during the rusting process. Then 5 % NaCl solution was poured into the corrosion trough as an electrolyte, stirring while pouring to ensure the uniformity of the solution until the liquid level was just over the tensile bars, with a height of about 20 mm. Corrosion in the RC beams was induced by using a constant DC voltage source (eTM-305F, 0–64 V, 0–5A). Tensile steel bars were made anode and connected to the positive terminal of power supply. Concrete was wrapped with a wire mesh outside, which was made cathode and connected to the negative terminal of power supply.

According to Faraday's second law, the theoretical mass loss of the tensile bars can be calculated, resulting in three specimen beams with varying corrosion levels. The mass loss can be determined using Eq. (1).

$$\text{Mass loss} = \frac{ItM}{Fn} \tag{1}$$

where I is the constant current passed (A); t is the time elapsed (s); M is the atomic weight (for iron: M = 55.84 g/mol); z is the ion charge; and F is Faraday's constant, equal to 96,485C/mol, which is the amount of

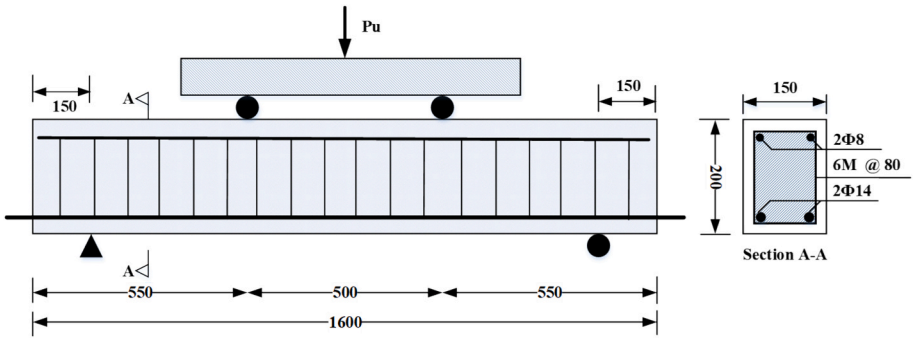

Fig. 1. Dimensions and reinforcement details of RC beams.

Table 1
Mechanical properties of steel bars, concrete and CFRP sheets.

Materials	Properties	Strength and strain(Mpa)	standard deviation (Mpa)	Elastic modulus (Gpa)
Concrete	Compressive strength	42.5	3.6	—
D14	Ultimate strength	615.7	16.2	200GPa
	Yield strength	462.2	5.5	
D8	Ultimate strength	611.3	15.2	200GPa
	Yield strength	408.9	4.5	
CFRP Sheets	Tensile strength	3000	—	230GPa
	Ultimate strain	1.66 %	—	

electrical charge in 1 mol of the metal.

As mentioned above, for mild, moderate and severe corrosion damage, accelerated corrosion cycles were 25, 50 and 100 days (5 %, 10 %, 20 %) in combination with continuous loading. For convenience, the uncorroded specimen beam and the other three corroded specimen beams with different corrosion levels were referred to US-0, CS-5, CS-10, CS-20, respectively.

2.3. CFRP anchorage system strengthening

As illustrated in Fig. 2, the manufacturing process of CFRP anchors involves a series of precise steps designed to ensure optimal performance [40]. First, CFRP sheets are cut into strips measuring 80 mm in length and 150 mm in width. These strips are then rolled along the sheet's texture to form carbon fiber bundles with a diameter of 8 mm. Next, the CFRP sheet is prepared for anchorage by securing the connecting wire at a designated depth of 35 mm, which facilitates proper bonding between the fiber bundle and the anchorage zone. The carbon fiber bundles are then impregnated with epoxy resin up to the anchorage depth, enhancing the bond between the CFRP and the concrete substrate. After the first impregnation, the epoxy resin is allowed to set, ensuring initial adhesion before a second impregnation is applied to further reinforce the bond. This multi-step process is critical to achieving a strong and durable connection between the CFRP anchors and the concrete structure.

The installation process of CFRP anchors for reinforcing RC beams following corrosion involves a series of carefully executed steps to ensure optimal bonding and structural performance. Initially, surface preparation is conducted by cleaning the concrete surface with an angle grinder to remove dust and contaminants, leaving it flat and dry to facilitate proper adhesion. Next, holes are drilled in the RC beams at the specified locations for the carbon fiber anchor placement, as illustrated in Fig. 3(a). It is crucial to clear the drilled holes of any debris or dust to create a clean bonding surface. Once the primer has solidified, the CFRP sheets are swiftly bonded to the surface of the RC beams. Epoxy resin is evenly applied to the CFRP sheet, and a roller is used along the fiber texture to eliminate air bubbles and ensure a smooth bond. The pre-drilled holes are then filled with epoxy resin, and the dowel end of the CFRP anchor is inserted to achieve full bonding, as shown in Fig. 3(b). The ends of the anchor are pressed firmly against the CFRP sheet to ensure thorough impregnation of the resin. After installation, the reinforced beams are left to cure at room temperature for seven days to allow the CFRP anchorage system to fully consolidate, as depicted in Fig. 3(c). This meticulous process results in enhanced structural reinforcement, significantly improving the durability and strength of RC beams, particularly after exposure to corrosion.

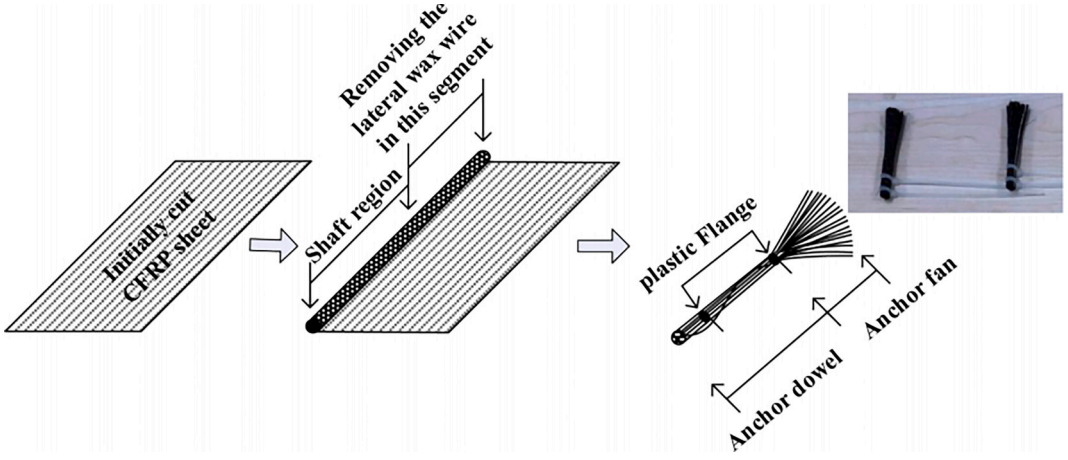

Fig. 2. Construction of CFRP anchors.

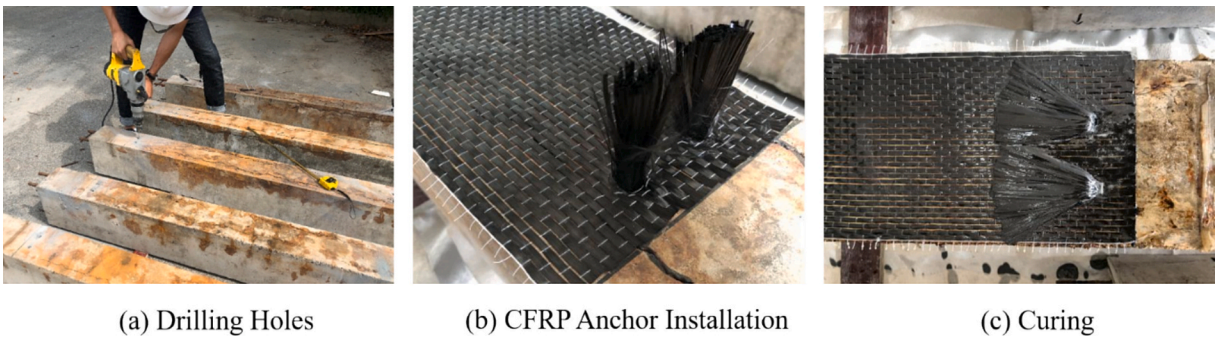

Fig. 3. The procedure of CFRP anchorage system installation.

2.4. Load testing and AE monitoring

In this study, the loading test was conducted at the Laboratory of Engineering Structural Performance Evolution and Control, Tongji University, utilizing an electro-hydraulic servo testing machine with a maximum load capacity of 2,000 KN. To ensure proper contact between the loading device and the RC beam, two pre-loading stages were performed before the formal loading, with the pre-loading value set at 5 % of the theoretically calculated ultimate load of the beam. Subsequently, a displacement-controlled loading scheme was employed, with a loading rate of 1 mm/min, until the specimen failed. During the loading process, high-definition cameras were strategically positioned on both sides of the loaded test beam to enable comprehensive recording of the entire process. This allowed for accurate observation and analysis of the crack development and failure mode of the RC beams. The loading device setup is presented in Fig. 4.

For Acoustic Emission monitoring, a standard monitoring setup was adopted, consisting of a digital AE data acquisition system (PCI-2) with 16 AE channels (Mistras Group, Inc), preamplifiers, AE sensors, and filters. The primary monitoring devices are depicted in Fig. 5. To enhance the induction of the AE sensors, five sensors were meticulously attached to the surface of each reinforced beam and securely bonded with iron sheets and epoxy adhesive. Specifically, as shown in Fig. 5, three sensors were evenly distributed near the top of the beam (two at the ends and one in the middle), while the remaining two sensors were positioned at the bottom of the beam to ensure comprehensive reception of the AE signals.

Before the actual AE monitoring commenced, the sensitivity of the AE sensors underwent verification using a pencil lead break test. During the flexural testing of RC beams corroded to different ages, AE signals were continuously recorded throughout the entire duration of loading. Initially, a threshold of 40 dB was set, with a preamplifier gain of 10 dB as input, to acquire the AE signals. The hit lock time and hit definition time were established at 300 μs and 1000 μs, respectively.

3. Data handling

3.1. Data filtering

The process of filtering AE signals in this study follows a systematic approach involving a combination of a Swansong-II filter, singular value decomposition (SVD), and discrete wavelet transform (DWT). Signal processing utilized Python with SciPy for SVD, PyWavelets for DWT, and custom Swansong-II thresholding. Clustering analysis employed scikit-learn GaussianMixture. SVD is mainly used in image compression, high-dimensional data visualization, and face recognition, etc. DWT is mainly used in JPEG 2000, signal/image denoising, feature extraction (multiscale), etc. The first step involves applying a duration-amplitude-based Swansong-II filter, as shown in Table 2, which effectively removes unwanted waveforms caused by sliding or mechanical rubbing. This amplitude-duration-based filtering method is widely adopted in various studies to enhance signal clarity by eliminating noise that does not meet predefined threshold conditions.

Following the initial filtering, singular value decomposition (SVD) is applied to further process the signal. The one-dimensional AE signal $x[n]$ is first transformed into a Hankel matrix X_{HM} of size $m \times n$, where the first row of the matrix is the original signal sequence, the second row is generated by shifting the signal vector one position to the right, and the process continues until the matrix is fully populated. The Hankel matrix X_{HM} is constructed as:

Fig. 4. Diagram of the loading device.

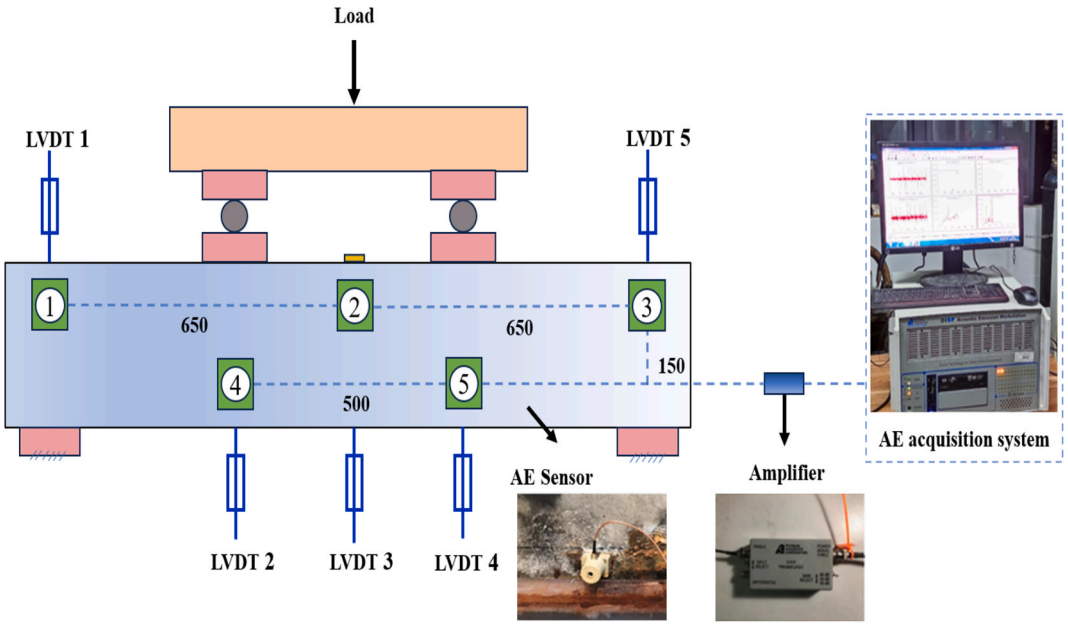

Fig. 5. Test setup for the AE health monitoring.

Table 2
Duration-Amplitude Filter (Swansong II).

Condition	Amplitude (dB)	Duration (μs)
1	40–45	<500
2	46–49	<650
3	50–53	< 820
4	54–56	<940
5	57–60	< 1000
6	60–67	<2000
7	68–75	<4000
8	76–83	<6000
9	84–91	< 8000
10	92–100	< 10,000

$$X_{HM} = \begin{pmatrix} x[1] & x[2] & \cdots & x[n] \\ x[2] & x[3] & & x[n+1] \\ \vdots & & \ddots & \vdots \\ x[m] & x[m+1] & \cdots & x[m+n-1] \end{pmatrix} \tag{2}$$

Next, the Hankel matrix is decomposed using SVD into the following form:

$$X_{HM} = USV^T \tag{3}$$

where U and V are orthogonal matrices of dimensions $m \times m$ and $n \times n$, respectively, and S is a diagonal matrix containing the singular values in descending order. Denoising is achieved by truncating the rank of the matrix to kkk, where k corresponds to the number of largest singular values that retain 90 % of the signal's energy. This truncation preserves the dominant features of the signal while discarding noise.

After SVD-based denoising, Discrete Wavelet Transform (DWT) is applied to further refine the signal by eliminating high-frequency noise, commonly referred to as "riding waves," and enhancing waveform symmetry. The DWT process decomposes the signal into approximation coefficients (low-frequency components) and detail coefficients (high-frequency components). The Daubechies wavelet (db10) is selected for this transformation, as it requires the fewest coefficients for signal reconstruction. The decomposed signal is represented as:

$$x(t) = \sum_k c_k \Phi_k(t) + \sum_{j,k} d_{j,k} \psi_{j,k}(t) \tag{4}$$

where $\Phi_k(t)$ are the approximation coefficients, $\psi_{j,k}(t)$ are the detail coefficients, and c_k and $d_{j,k}$ are the corresponding low and high-frequency coefficients. By retaining only the most significant coefficients, the signal is reconstructed to effectively eliminate high-frequency noise while preserving essential features.

3.2. Data Smoothening

In the analysis of AE data, effective noise reduction and trend identification are essential for accurate interpretation of structural behavior. Double exponential smoothing, commonly referred to as Holt's linear trend method, is well-suited for this purpose as it accommodates both the level and trend components of time-series data. This method provides a more nuanced smoothing technique compared to simple exponential smoothing, which accounts only for the data's level.

Let y_t represent the observed AE signal at time t. The method introduces two key components: the level l_t, which reflects the smoothed value of the signal, and the trend b_t, which captures the rate and direction of change over time. The smoothing process is governed by two recursive equations.

First, the level at time t is updated using the following equation:

$$l_t = \alpha y_t + (1-\alpha)(l_{t-1} + b_{t-1}) \tag{5}$$

Here, l_t denotes the updated level, y_t is the current observation, l_{t-1} is the previous level, and b_{t-1} is the prior trend. The smoothing parameter α determines the weight given to the most recent observation compared to the previous level estimate. A higher α makes the smoothing process more responsive to recent data, while a lower α yields a more stable estimate, smoothing out short-term fluctuations.

Next, the trend at time ttt is adjusted based on the difference between the current and previous levels:

$$b_t = \beta(l_t - l_{t-1}) + (1-\beta) b_{t-1} \tag{6}$$

In this equation, b_t represents the updated trend, and β $(0 < \beta < 1)$ controls how much weight is assigned to the recent changes in the level. A higher β results in a trend that quickly adapts to changes in the data, while a lower β produces a more gradual trend, which is less affected by short-term variations.

For this study, smoothing parameters were carefully selected: $\alpha = 0.8$ and $\beta = 0.2$. These values were chosen to balance the sensitivity of the

smoothing process to recent observations with the need for a stable trend. This combination ensures that the signal's underlying structure is preserved while minimizing the influence of noise.

4. Results of mechanical properties

4.1. Load capacity

During the monotonic four-point loading test, the mid-span deflection of the four specimen beams was carefully recorded. The load–deflection curves of the test beams are presented in Fig. 6. Notably, the flexural response of the CFRP-strengthened beams exhibited a consistent pattern, closely related to the duration of accelerated corrosion, i.e., the degree of corrosion of the specimen beams. As observed in Fig. 6, the load capacity of the specimen beams gradually decreased with increasing degrees of corrosion, narrowing the performance gap between adjacent specimens. Table 3 provides a summary of the yield load P_y and ultimate load P_u of all specimen beams. A comparison with the pristine specimen beam (US-0) revealed that the yield load and ultimate load of corroded beams (CS-5, CS-10, CS-20) decreased by 12 %, 23 %, 19 % and 6.0 %, 14 %, 22 %, respectively.

4.2. Ductility index

To assess the flexural ductility of the specimen beams, the flexural ductility index (ΔI) was calculated by taking the ratio of the mid-span deflection at the ultimate point (δ_u) to the mid-span deflection at the yield point (δ_y). The flexural ductility index for each specimen beam is presented in Table 4. It is observed that the yield deflection (δ_y) initially decreased and then increased, while the ultimate deflection (δ_u) continued to increase with increasing levels of corrosion. Moreover, compared to the pristine specimen beam (US-0), specimen beam CS-5 and CS-10 exhibited significantly improved ductility performance, with enhancements of 11.0 %, and 20.0 %, respectively. However, the ductility performance of specimen beam CS-20 decreased by 26 %. In the mild corrosion range (≤10 %), corrosion product-filled microcracks synergize with the anchoring system to increase the specimen beam ductility index (ΔI), with CS-10 exhibiting the highest ductility due to the optimal failure mode (progressive debonding), but this increase in ductility is an unsustainable pseudo-safety; at corrosion rates of up to 20 %, the loss of rebar cross-section with pre-damage resulted in an inverse decrease in ductility of 26 %.

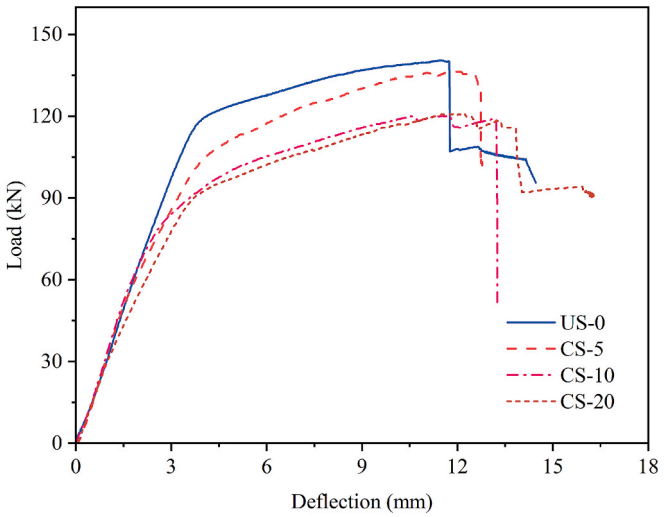

Fig. 6. Load–deflection curves of specimen.

Table 3
Summary of the test results.

Beams	P_y(KN)	P_u(KN)	$P_{y_{Nor}}$[a](KN)	$P_{u_{Nor}}$[a](KN)	Mode of failure
US-0	119.5	140.5	1.00	1.00	CCS
CS-5	104.8	131.4	0.88	0.94	CD-AP
CS-10	92.6	121.2	0.77	0.86	CD-AP
CS-20	97	109.8	0.81	0.78	MC-FR

[a] Normalized in relation to the beam US-0.

Table 4
Ductility of the CFRP strengthened beams.

Beams	Mid-span displacement(mm)		Ductility index	
	δ_y(mm)	δ_u(mm)	ΔI	ΔI_{Nor}[a]
US-0	4.03	11.68	2.59	1.00
CS-5	3.86	12.36	3.20	1.11
CS-10	3.82	13.25	3.47	1.20
CS-20	4.00	8.46	2.12	0.73

[a] Normalized in relation to the beam US

4.3. Failure modes

Table 3 illustrates the three primary failure modes observed in the four specimen beams, namely, concrete cover separation (CCS), debonding of CFRP sheet followed by pulling out of anchors (CD-AP) and matrix cracking and fiber tearing (MC-FT), as depicted in Fig. 7. A detailed description of these three failure modes is provided below. The CCS failure mode was observed in specimen beams US-0. In this mode, extensive spalling of the concrete cover at the bottom of the beams was evident. Notably, no debonding was observed at the interface between the CFRP sheet and the concrete. The failure exhibited a more brittle behavior, likely due to the interconnected corrosion cracks and flexural cracks, leading to the detachment of concrete at the bottom.

The CD-AP failure mode was observed in specimen beams CS-5 and CS-10, where debonding occurred between the CFRP and concrete matrix near the end of the sheet, followed by anchor pull-out in close proximity. The debonding in the CD-AP mode was initiated by the propagation of bending cracks into the thin layer of the substrate, coupled with the relative deformation between the CFRP and the concrete matrix. It is crucial to note that the anchors played a vital role in retarding the debonding of the fabric, resulting in a shift from brittle cover separation to a more progressive debonding of the fabric. As a result, the specimen beams showed higher ductility in contrast to those that failed due to concrete cover separation (CCS).

The MC-FT failure mode of concrete matrix cracking and fiber tearing involves CS-20 beam with high degree of corrosion. As load increased in this failure mode, cracking began gradually in the concrete matrix at the interface between the CFRP sheet and concrete, followed by the tearing of CFRP sheet. Unlike other failure modes, no interface stripping or anchor pulling was observed during this process, and the tearing of CFRP sheets mainly occurred near the loading point. This failure mode is mainly due to the span stress concentration of CFRP sheets caused by concrete cracks, indicating that the failure risk of CFRP reinforced beams may be directly determined by the material strength under high corrosion conditions.

5. Results of AE monitoring

5.1. AE ringing counts analysis

The AE ringing counts refer to the total number of signals that exceed the threshold within a single AE hit. It is an important indicator of the activity of the AE phenomenon and is related to the magnitude of the threshold value. Studies have concluded that using AE ringing count to characterize multiple parameters of AE signal characteristics can better

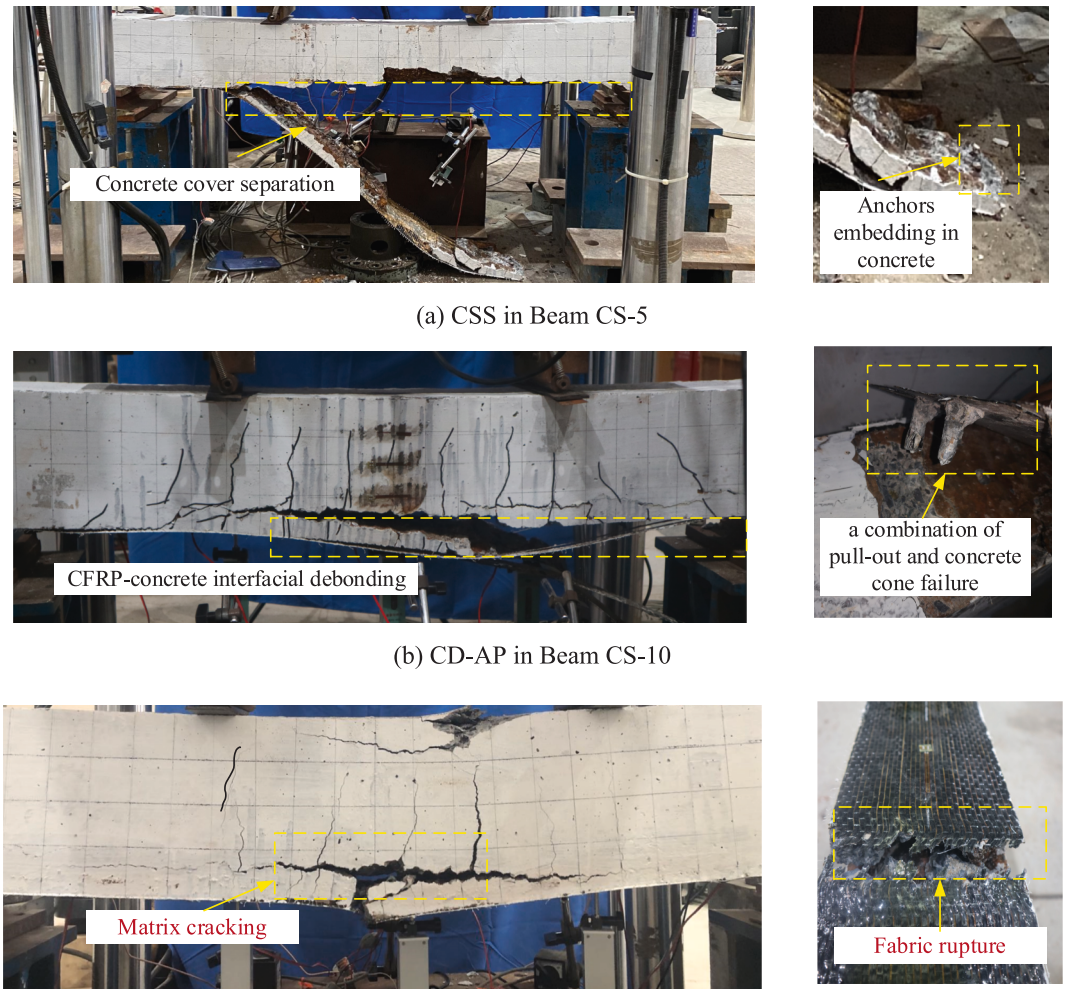

Fig. 7. Modes of failure.

reflect the changes in material properties because the AE ringing counts are proportional to the strain energy released during material damage [25,41,42]. Therefore, AE ringing counts and cumulative AE ringing counts are used in this study to characterize the entire damage process of CFRP-strengthened RC beams.

Fig. 8 illustrates the loading behavior of CFRP-strengthened reinforced concrete beams subjected to varying levels of corrosion, represented through AE activity and corresponding load-time curves. The data analysis in Fig. 8 divides the loading process into three distinct stages: the initial damage stage (Stage I), the damage development stage (Stage II), and the continuous damage stage (Stage III). This classification aids in a better understanding of the influence of corrosion on beam performance.

In Stage I (Initial Damage Stage), Fig. 8(a) shows that AE signal intensity remains low, and cumulative AE counts exhibit a slow increase, indicating that the concrete structure primarily undergoes initial elastic deformation. At this stage, microcracks and voids may undergo compression or closure, but no significant damage is observed. From the figure, the AE activity for the uncorroded beam (US-0) and corroded beams is similar during this phase, suggesting that corrosion has minimal influence on internal damage during initial loading. In Stage II (Damage Development Stage), AE activity increases markedly, with cumulative AE counts rising sharply, particularly in beams with corrosion levels of 5 %, 10 %, and 20 %, where the curves exhibit a steeper slope. This indicates a significant acceleration in the initiation and propagation of cracks within the concrete matrix, as well as possible localized debonding at the CFRP-concrete interface. As the load continues to increase, the beam's stiffness gradually decreases, with more pronounced visible cracking, especially in beams with moderate to severe corrosion (e.g., CS-10 and CS-20). It is evident from the figure that higher corrosion levels lead to a more rapid increase in AE counts, reflecting the accumulation of more severe internal damage. During Stage III (Continuous Damage Stage), the cumulative AE count continues to increase, though at a slower rate compared to Stage II, indicating that the internal cracks are approaching a saturation point and the failure mechanisms are stabilizing. The figure shows that, following the peak load, the uncorroded beam maintains relatively high load-bearing capacity, while corroded beams exhibit a significant reduction in peak load, especially for the CS-20 beam, which demonstrates a rapid drop after reaching its peak. This behavior indicates accelerated failure of the structure. Notably, severe corrosion (20 %) leads to premature failure at lower load levels, accompanied by increased AE activity, indicating intensified damage processes such as concrete matrix cracking, CFRP tearing, and interface debonding.

From Fig. 8, it is evident that corrosion has a substantial adverse impact on the overall performance of CFRP-strengthened beams, particularly under moderate to severe corrosion conditions. As the corrosion level increases, AE activity during Stages II and III rises significantly, with the cumulative AE count curves becoming increasingly steeper, suggesting more aggressive crack initiation and

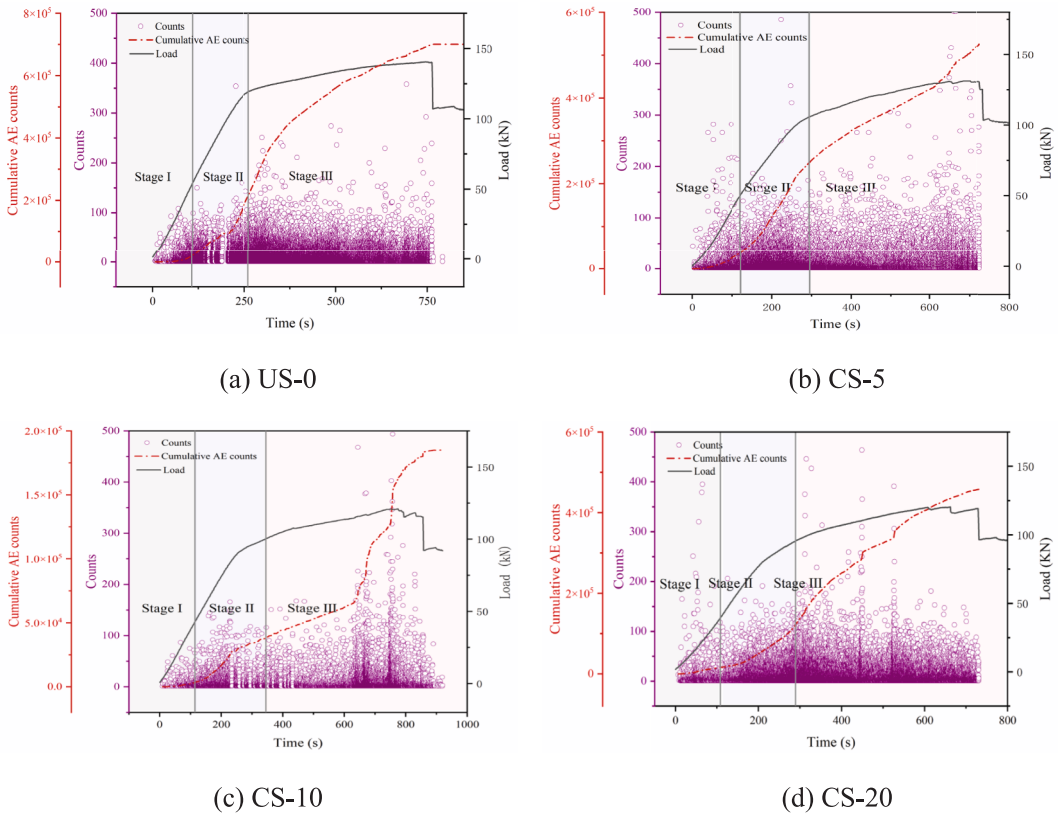

Fig. 8. Variation characteristics of the cumulative AE ringing counts and loads over time for CFRP beams with four levels of corrosion.

propagation, and accelerated damage accumulation. Furthermore, as corrosion levels rise, the peak load shows a noticeable decrease, with the CS-20 beam exhibiting the most significant reduction. This can be attributed to the reduction in steel reinforcement cross-sectional area due to corrosion, as well as the weakening of the bond between the steel and concrete, which in turn accelerates structural damage, reduces stiffness, and decreases load-bearing capacity. These observations underscore the detrimental effects of corrosion on the performance of CFRP-strengthened beams, especially in accelerating crack growth and reducing structural integrity. The results emphasize the importance of effective corrosion mitigation measures to maintain the durability and stability of CFRP-reinforced concrete structures over long-term service.

5.2. AE intensity analysis

Signal intensity analysis is a deeper analysis of the acoustic emission data. This method has been applied to evaluate the damage levels in RC beams. In order to analyze the intensity of the acoustic emission damage source, the severity value S_r of the acoustic emission signal and the historical index HI recorded by the system are calculated, and the changes in their values are analyzed and graphically represented visually [43–45].

The severity S_r is defined as the average signal intensity of the J acoustic emission signals that exhibit the maximum signal intensity up to moment t and can be calculated based on Eq. (7).

$$S_r = \sum_{i=1}^{J} \frac{S_{oi}}{J} \tag{7}$$

where S_{oi} is ith most enormous acoustic emission signal intensity value up to moment t; J is an empirical constant related to the material types and crack mechanism of specimens. For concrete structures, if J is less than 50, then J equals 0; if $J > 50$, J equals 50. Eq. (7) indicates that the value of S_{oi} is counted from the 51st received acoustic emission signal.

The history index HI is determined from the ratio of the average signal intensity of the last K AE events to the average signal intensity of all measured AE events and was obtained by using Eq. (8). This indicates that the value of HI in the first 50 acoustic emission signals is 1.

$$HI = \frac{\sum_{i=N-K+1}^{N} \frac{S_{oi}}{K}}{\sum_{j=1}^{N} \frac{S_{oi}}{N}} \tag{8}$$

Where N is the number of AE hits from the start of loading to moment t; S_{oi} is the signal intensity of the ith AE event; K is an empirical factor related to N, and can be chosen according to Eq. (9).

$$K = \begin{cases} 0, N \le 50 \\ N - 30, 50 < N \le 200 \\ 0.85N, 200 < N \le 500 \\ N - 75, N > 500 \end{cases} \tag{9}$$

Large concrete cracks and CFRP fabric damage produced AE signals with significant energy. As expected from Eq. (7), the S_r value tends to increase when the damage occurs with a signal intensity higher than the previous 50 maximum AE signal intensities.; When the signal intensity of the new damage is less than the previous 50 maximum AE signal intensities, the S_r value remains unchanged. Therefore, the sudden increase in S_r value represented that some form of damage was occurring in the CFRP-strengthened beams.

Fig. 9 shows the graphs of cumulative signal strength, S_r and HI with time under the condition of gradually increasing load. It can be observed that the changes in CSS and S_r of the specimens with different corrosion levels exhibit clear patterns during the loading process. CSS and S_r are key indicators for assessing crack propagation and damage accumulation, and their changes are directly related to the occurrence, development, and debonding of CFRP. For the uncorroded beam (US-0), CSS gradually increases in the early loading stage, while the S_r remains stable during the initial crack initiation phase, indicating that the cracks

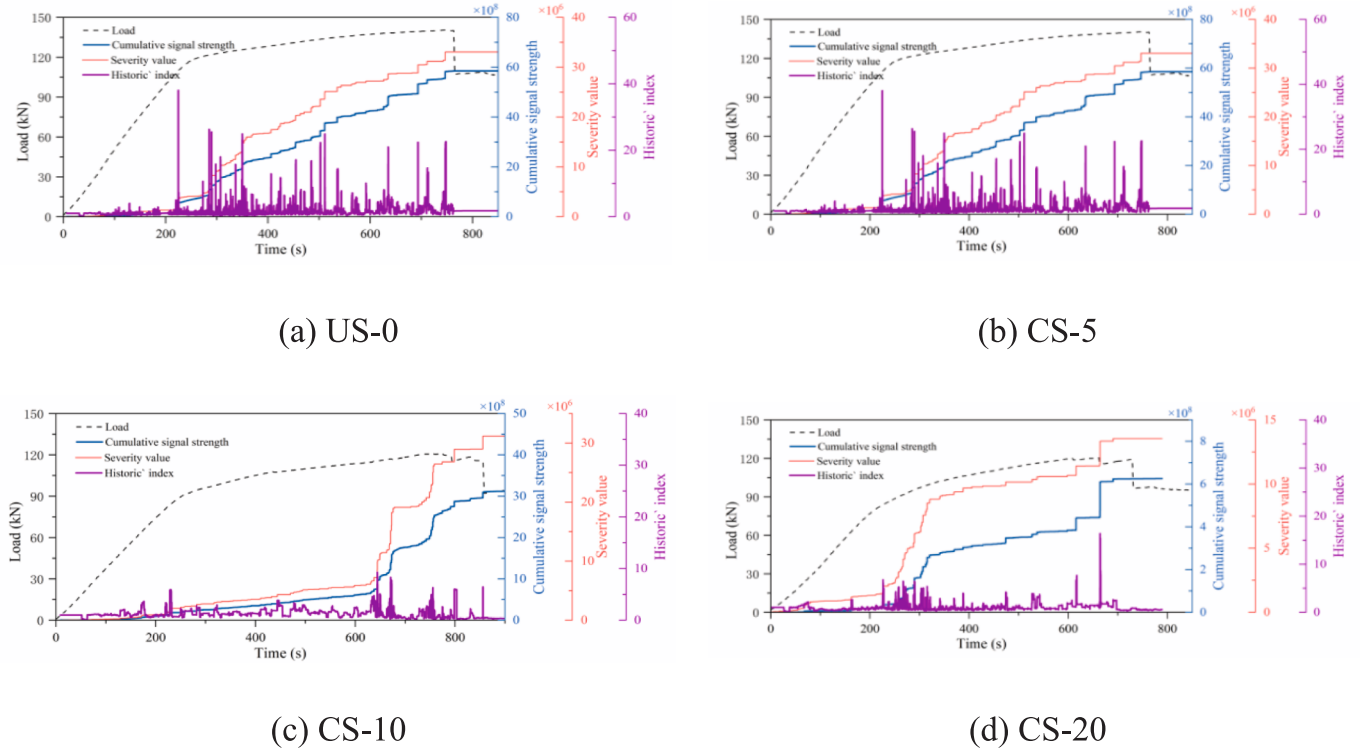

Fig. 9. Variation of S_r, *HI* and cumulative signal strength of CFRP beams with 4 levels of corrosion.

are still in the early stage of development. Between 450 s and 550 s, there is a significant increase in both CSS and S_r, corresponding to crack propagation and CFRP debonding, especially as the cracks start to expand significantly, leading to an increased release of energy. In the lightly corroded beam (CS-5), CSS and S_r exhibit a substantial increase in the late loading stage (after 600 s), indicating that crack propagation severity intensifies, with CFRP debonding and transverse cracks in concrete becoming the main sources of energy release during the crack expansion process. For the moderately corroded beam (CS-10), both CSS and S_r are relatively low during the early loading stage, reflecting the inhibition of initial crack growth due to corrosion. However, between 600 s and 700 s, as loading continues, the cracks begin to propagate rapidly, resulting in significant increases in both S_r and CSS. This suggests that under corrosion conditions, CFRP reinforcement debonding and tearing influence crack propagation. In the heavily corroded beam (CS-20), both CSS and S_r remain at low levels throughout the loading process, indicating that cracks had almost fully developed before loading, thus significantly restricting further crack growth and energy release in the subsequent stages. The debonding and tearing of CFRP also played a role in inhibiting energy release.

The historic index (*HI*) reflects the level of crack activity, particularly the accumulation and progression of damage. From Fig. 9, it can be seen that the changes in HI also exhibit distinct patterns across different specimens. For the uncorroded specimen (US-0), HI remains relatively stable during the initial loading stage but increases significantly between 450 s and 550 s, indicating a high level of crack activity and intensified damage propagation. In the late stage, further crack growth results in more energy release, consistent with the substantial increase in CSS and S_r curves. In the lightly corroded specimen (CS-5), HI shows significant fluctuations during the middle and late stages, especially after 600 s, reaching its highest value, which suggests increased crack activity. The presence of light corrosion accelerates crack initiation and development. In the moderately corroded specimen (CS-10), HI remains stable during the early loading stage but fluctuates significantly in the late stage, indicating that the initial crack growth is inhibited by corrosion, but crack activity increases as loading continues. In the heavily corroded specimen (CS-20), HI remains at a low level throughout the loading process, with a maximum value of only 15, indicating that cracks were highly developed before loading, resulting in reduced crack activity in the subsequent stages. This trend is consistent with the low levels observed in CSS and S_r.

5.3. *B-value analysis*

The b-value was first proposed by Gutenberg and Richter as a parameter for predicting the likelihood of an earthquake above a specific magnitude, and has been widely used in quantitative analysis of seismic activity. The Gutenberg-Richter formula is shown below Eq. (10).

$$\log_{10}N = a - bM \tag{10}$$

where M is the Richter magnitude of the earthquake; N is the number of earthquakes with magnitude exceeding M; a and b are empirical constants respectively representing the intercept and slope between earthquake magnitude and earthquake frequency via regression analysis.

The b-value in seismology characterizes the relationship between magnitude and frequency, and its trend is closely related to the development of internal cracks in concrete.[46–50] As a by-product during material damage, AE elastic waves are very similar in principle to seismic waves. Thus Eq. (11) was modified by substituting AE amplitude for seismic magnitude as follows:

$$\log_{10}N = a - b\left(\frac{A_{dB}}{20}\right) \tag{11}$$

Where A_{dB} is the magnitude of the AE signals; N is the number of AE signals with a magnitude exceeding A_{dB}; a and b, representing the intercept and slope, are the regression parameters of AE events.

The *Ib*-value which was developed from the b-value was applied in in the civil engineering field recently. Doyun jung et al. [51] investigated the effect of different locations of AE sensors on the changes of *Ib*-value

of epoxy composites, the results showed that the *Ib*-value could serve as a valid indicator reflecting the composite structure states. The team further used the b-value and *Ib*-value in the AE signals to analyze the failure behaviour of FRP composites, indicating that the Ib-value enables faster and more effective analysis of structural abnormalities[52].

The *Ib*-value is a statistical value calculated from AE events and can be obtained by following Eq. (12):

$$Ib = \frac{\log_{10}N(\mu - \alpha_1 \bullet \sigma) - \log_{10}N(\mu + \alpha_2 \bullet \sigma)}{(\alpha_1 + \alpha_2) \bullet \sigma} \tag{12}$$

Where μ and σ are mean and standard deviation of the amplitude distribution in recency N AE signals; α_1 and α_2 are usually constants between 0 and 1. In this study α_1 and α_2 are set to 1 and N is set to 50.

The *Ib*-value is a transient feature updated with each newly recorded AE signal during material cracking, which can be applied to effectively differentiate between damage types throughout the loading process. The change of the *Ib*-value of AE reflects the initiation, expansion and evolution of cracks inside the material. Higher Ib-values (> 0.1) indicate the smaller scales and minor damage, there are more low-amplitude signals in the AE signals, which shows the structure is in the microcrack expansion stage. Lower Ib-values (< 0.75) mean the greater scales and more severe damage, there are more high-amplitude signals and the structure is mainly in the macroscopic crack expansion stage. When the *Ib*-value fluctuates up and down in a relatively stable range, it indicates that the structure is in a relatively stable expansion stage.

Fig. 10 illustrates the magnitude strength, *Ib*-value curves and loading curves for four CFRP-reinforced beams with different levels of corrosion. From the Ib-value curves, it can be observed that the beams with no corrosion (US-0) and slight corrosion (CS-5) exhibit similar trends, while the beams with moderate corrosion (CS-10) and severe corrosion (CS-20) share another similar pattern. This suggests that different corrosion levels lead to distinct damage behaviors in these beams. For the non-corroded (US-0) and lightly corroded (CS-5) beams, during the initial phase (Stage I), the Ib-value remains at a low and stable level, indicating that the structure is primarily undergoing elastic deformation with minimal crack formation and internal damage. As loading progresses into Stage II, the Ib-value starts to show significant fluctuations and a sharp increase, marking the initiation and propagation of internal cracks and accelerated damage accumulation. This phenomenon is particularly evident in CS-5, where the intense fluctuation of the Ib-value persists for a longer duration and exhibits higher amplitude compared to US-0. This suggests that light corrosion may enhance the ductility of the beam, allowing for extended crack propagation and greater energy absorption during this stage. This enhanced ductility might be due to changes in the bond behavior between the steel reinforcement and the concrete caused by light corrosion, enabling the structure to absorb more deformation energy during crack propagation. Moving into Stage III, the Ib-value gradually decreases in amplitude and becomes more stable, indicating that the crack development is reaching saturation, damage accumulation is slowing down, and the structure is approaching failure.

In contrast, the moderately corroded (CS-10) and severely corroded (CS-20) beams exhibit a different damage evolution pattern. Throughout the entire loading process, these specimens show Ib-values that fluctuate sharply but without prominent peaks at higher levels, suggesting that extensive corrosion in the early stages has caused the cracks to nearly fully develop at the beginning of the loading process, leading to limited further crack propagation. It is notable that the fluctuation intensity and amplitude of the Ib-value for CS-10 are significantly higher than those

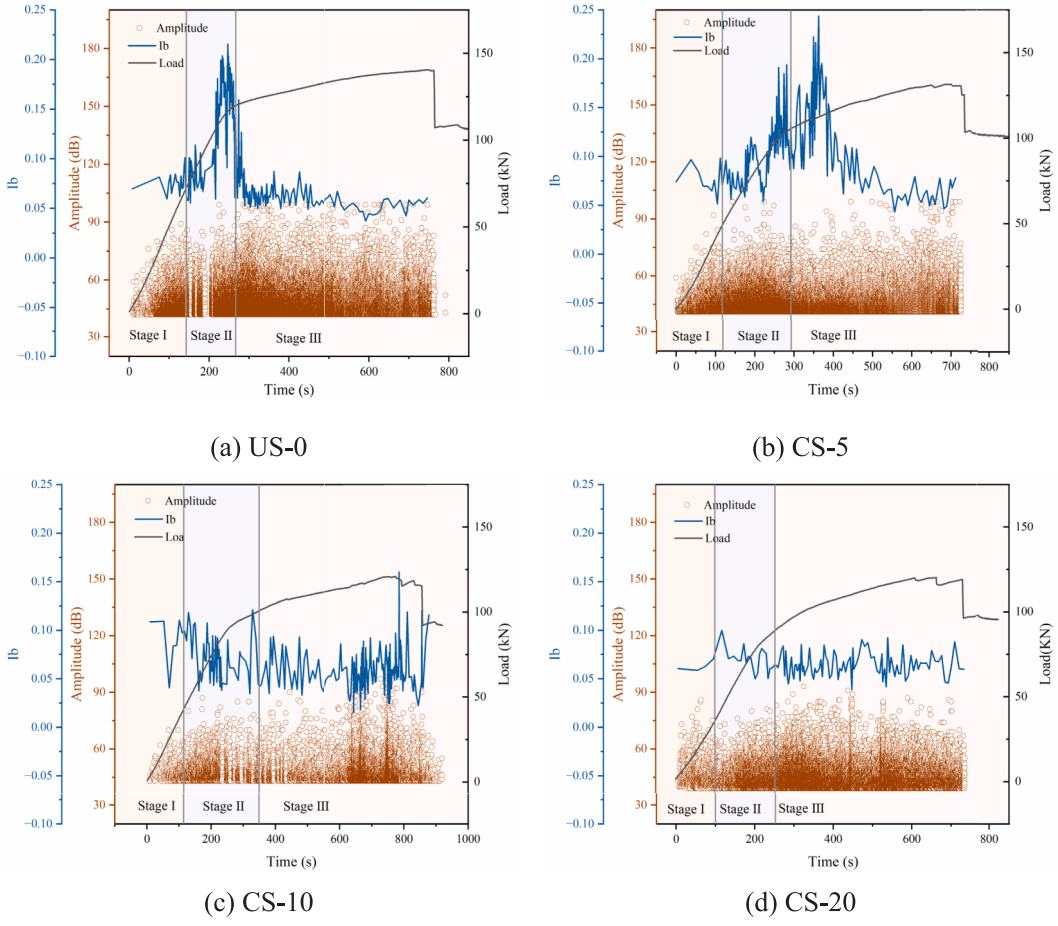

Fig. 10. Variation of *Ib* values and amplitudes of CFRP beams with 4 levels of corrosion.

for CS-20. This could be attributed to two factors: the more severe corrosion in CS-20, which results in a reduced cross-sectional area of the steel reinforcement and consequently lower load-carrying capacity, and the relatively better ductility of CS-10, which allows for more significant crack development.

5.4. RA-AF crack classification

The concrete structures in service are subjected to external forces, leading to failures mainly involving the initiation, expansion, and penetration of internal micro-cracks. The development of these cracks includes two types, tensile and shear cracks, whose relative proportions change with increasing forces during the structural loading process.

To more accurately classify cracks during the damage process, the parameter analysis method proposed by JCMS-III b5706 has become a key tool. This method, through the analysis of acoustic emission parameters, yields two crucial parameters, RA and AF, as defined by Eq. (13) and Eq. (14), respectively:

$$\mathrm{RA} = \frac{\text{Rise time}}{\text{Maximum Amplitude}} \tag{13}$$

$$\mathrm{AF} = \frac{\text{Ring counts}}{\text{Duration}} \tag{14}$$

As illustrated in Fig. 11, scatter plots using RA and AF data provide a method for crack classification. According to the crack classification method of JCMS-III b5706, signals with low RA values and high AF features suggest the initial formation or through-thickness propagation of tensile cracks. Conversely, high RA values and low AF features generally indicate the early stages or through-thickness extension of shear cracks. This classification method enables accurate crack type identification at the onset of material failure, supporting more precise damage diagnosis.

In addition to analyzing AE signals, observing macroscopic failure characteristics enables a more comprehensive understanding of the internal formation and development of cracks. This integrated research approach offers a deeper insight into crack analysis in structural engineering, helping to predict and prevent potential structural damages, and providing practical and reliable technical support for engineering practices.

In recent years, scholars have employed Gaussian Mixture Clustering to classify tensile and shear cracks obtained from acoustic emission experiments, overcoming the shortcomings of traditional crack classification, which was ambiguous along the diagonal classification method.

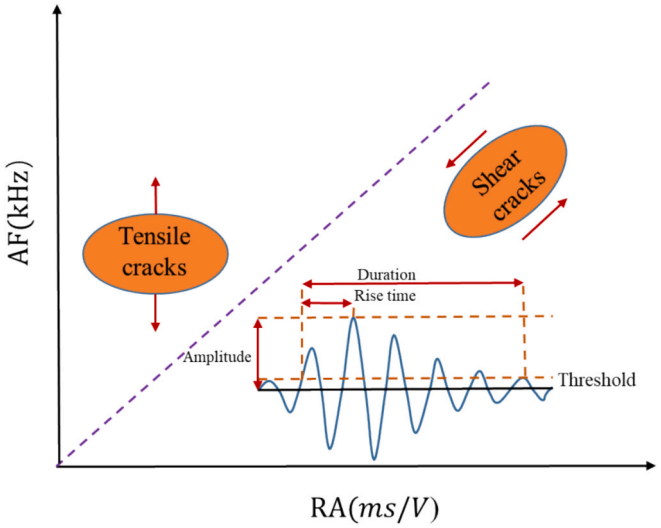

Fig. 11. Crack Mode Classification.

Gaussian Mixture Clustering, a probabilistic model-based classification method, is particularly suitable for handling multidimensional and complex datasets. Gaussian Mixture Clustering (GMM) was applied with 2 components (corresponding to tensile and shear cracks), initialized using the k-means++ method to improve convergence stability. Not only does it reveal the probability of each data point belonging to different clusters, but it also adapts to diverse data structures, making it especially effective in complex data analyses, such as crack classification in acoustic emission monitoring.

In the four-point bending test, the clustering calculation of AE signals through the Gaussian Mixture Model (GMM) algorithm effectively segregates the tensile and shear cracking signals during the loading process of beams reinforced with a new type of FRP anchoring system. The classification results of tensile and shear cracks in each reinforced concrete beam are shown respectively. It is observed that the degree of steel reinforcement corrosion has a relatively limited impact on the classification of the two types of cracks. For tensile cracks, the RA values usually range between 500 to 7000 ms/V, while the average frequency AF is between 0 to 200 kHz. For shear cracks, RA values lie between 0 to 500 ms/V, with an average frequency AF ranging from 0 to 80 kHz. The characteristic features of shear cracks are higher RA values and lower AF values.

Fig. 12 illustrates the distribution of tensile and shear cracks at different damage stages of the test beams, highlighting the evolution of crack patterns within the concrete matrix of beams reinforced with the CFRP anchoring system during four-point bending. The results clearly indicate that the number of tensile crack events is substantially higher compared to shear crack events, suggesting that the structural response under loading is predominantly characterized by tensile failure. Moreover, during the continuous damage stage, the number of both crack types increases significantly, surpassing those observed during the initial damage and damage development stages. This observation corresponds with the finding that crack propagation predominantly intensifies during the continuous damage phase.

Table 5 presents the proportions of shear and tensile cracks at three distinct stages (initial damage, damage development, and continuous damage) for reinforced beams with varying levels of corrosion (0 %, 5 %, 10 %, 20 %). During the initial damage stage, the beam without corrosion (US-0) exhibits a baseline shear crack proportion of 10.04 %, with fluctuations observed as corrosion advances. For slightly corroded beams (CS-5), the initial shear crack proportion is reduced to 8.64 %, which may indicate a marginal initial positive effect of mild corrosion on the structural response. However, as the corrosion level increases to 10 % and 20 %, the shear crack proportions rise to 15.67 % and 17.98 %, respectively, indicating that higher levels of corrosion degrade the bond between steel and concrete, thereby promoting the formation of shear cracks. During the damage development stage, the shear crack proportion in the US-0 beam increases slightly to 15.08 %, whereas the CS-5 beam experiences a more pronounced increase to 17.76 %, suggesting that even mild corrosion has begun to demonstrate destructive effects under sustained loading. The shear crack proportion continues to increase in the CS-10 beam, reaching 18.99 %, and rises slightly further in the CS-20 beam to 19.43 %, affirming a positive correlation between corrosion severity and shear crack formation. In the continuous damage stage, all samples exhibit a substantial increase in the proportion of shear cracks. The US-0 beam reaches a shear crack proportion of 22.97 %, while the CS-5 beam rises to 23.52 %. The moderately corroded CS-10 beam further increases to 26.65 %, indicating the detrimental impact of corrosion on structural integrity. The severely corroded CS-20 beam reaches the highest shear crack proportion of 30.62 %, reflecting significant damage to the shear load-carrying capacity at elevated corrosion levels. Overall, the results clearly demonstrate that corrosion significantly influences the formation of shear cracks in reinforced concrete beams, with this impact becoming increasingly pronounced as the corrosion level escalates. Notably, at higher corrosion levels, a marked increase in shear crack proportion is evident, highlighting the

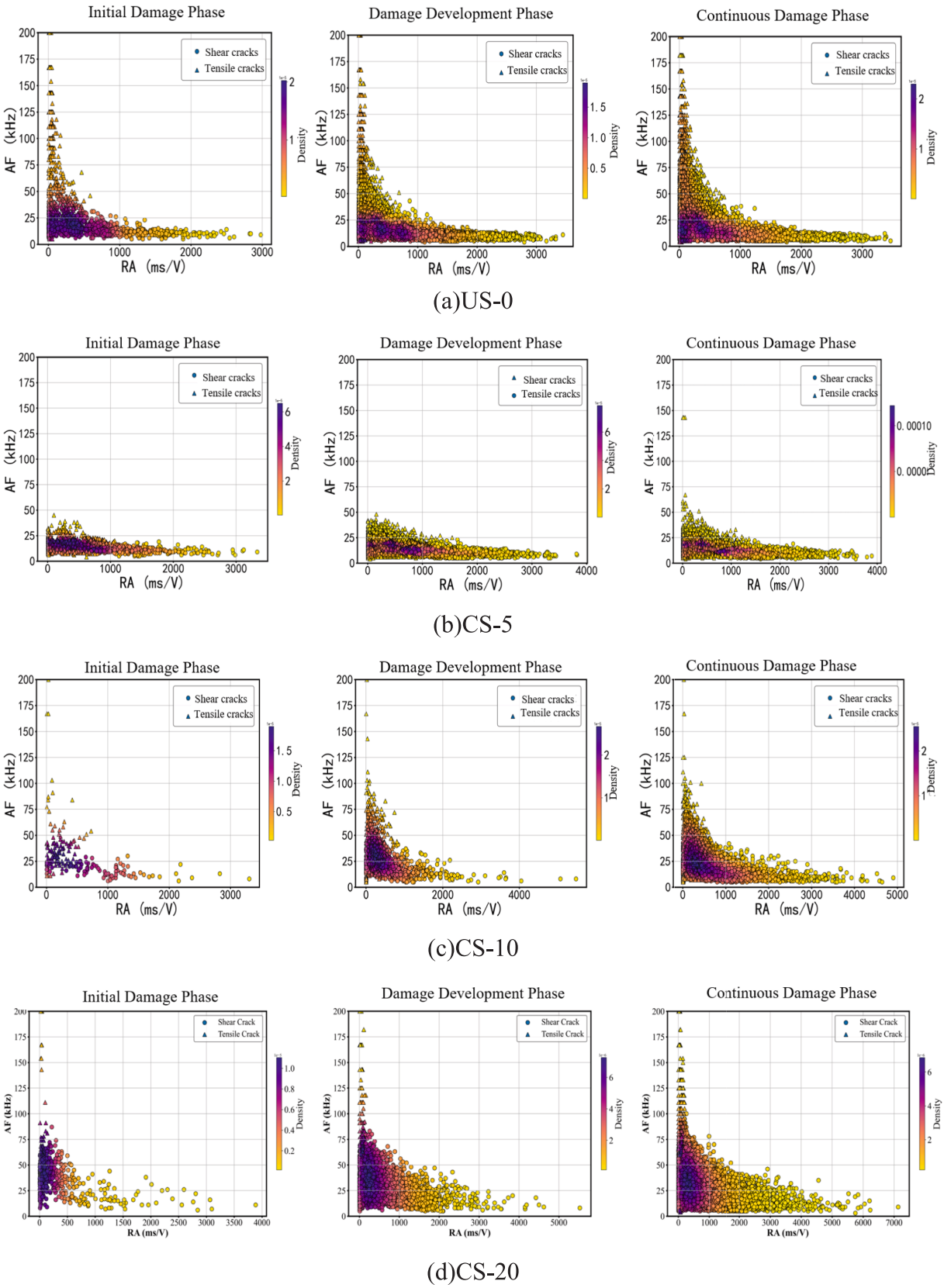

Fig. 12. Tensile and shear crack distribution of CFRP beams at different damage stages for four corrosion levels.

Table 5
Ratio of shear cracks to tensile cracks at different stages of test beams.

Beams	Initial damage stage		Damage development stage		Continuous damage stage	
	Tensile crack rate	Shear crack rate	Tensile crack rate	Shear crack rate	Tensile crack rate	Shear crack rate
US-0	89.96 %	10.04 %	84.92 %	15.08 %	77.03 %	22.97 %
CS-5	91.36 %	8.64 %	82.24 %	17.76 %	76.48 %	23.52 %
CS-10	84.33 %	15.67 %	81.01 %	18.99 %	73.35 %	26.65 %
CS-20	82.02 %	17.98 %	80.57 %	19.43 %	69.38 %	30.62 %

severe effect of corrosion on structural performance.

While uncertainties in sensor placement and small sample size exist, the quantitative RA-AF thresholds and Ib-value trend consistency provide a robust foundation for field monitoring. By integrating GMM clustering into SHM protocols, engineers can transition from reactive to predictive maintenance, leveraging AE's non-destructive, real-time capabilities to extend the service life of corroded structures.

6. Conclusions

This study focused on the AE-based health monitoring of RC beams subjected to corrosion and strengthened with a CFRP anchorage system under bending loads. By employing AE monitoring techniques alongside crack classification methods, the research systematically examined the damage evolution and crack behavior across various corrosion levels. Key indicators such as AE ringing counts, signal intensity, Ib-value and RA-AF crack classification were analyzed, leading to the following conclusions:

(1) Three typical failure modes were observed in the CFRP-strengthened corroded beams: concrete cover separation, debonding of CFRP sheet followed by pulling out of anchors, and matrix cracking and fiber tearing. CFRP anchorage system made a great contribution to the improvement of pre-yield stiffness and ultimate strength of specimen beams at a lower corroded level. A comparison of the yield loads of CS-5, CS-10, and CS-20 with those of US-0 reveals a decline of 12 %, 23 %, and 19 %, respectively. Concurrently, the ultimate loads exhibited a decrease of 6.0 %, 14 %, and 22 %, respectively.

(2) AE ringing counts analysis effectively revealed the damage evolution of CFRP-strengthened beams during loading. Based on the cumulative AE ringing counts curves, the bending failure of CFRP-strengthened beams can be divided into three stages: initial damage stage, damage development stage, and continuous damage stage.

(3) Signal intensity (S_r) and historic index (HI) analyses provided further insight into damage severity and crack activity. In uncorroded beams, S_r and HI showed gradual increases, whereas in corroded beams, significant fluctuations in HI indicated enhanced crack propagation and CFRP debonding. Severe corrosion reduced the intensity and frequency of AE signals in the late loading stage, suggesting that initial crack activity was inhibited, while increased AE activity in the middle and late stages correlated with accelerated damage in beams with mild to moderate corrosion.

(4) The Ib-value, calculated from AE amplitude distribution, showed distinct trends depending on the corrosion level. Beams with little or no corrosion exhibited Ib-value fluctuations corresponding to different damage stages, with higher ductility observed in mildly corroded specimens. In contrast, heavily corroded beams maintained low Ib-values due to extensive initial crack formation, indicating limited further damage development under load. These findings support the use of Ib-value as a reliable indicator of structural integrity and damage severity in CFRP-reinforced beams.

(5) The RA-AF crack classification method, along with Gaussian Mixture Clustering, was used to differentiate tensile and shear cracks. The results indicate that in the initial damage stage, the proportions of shear cracks in US-0, CS-5, CS-10, and CS-20 beams were 10.04 %, 8.64 %, 15.67 %, and 17.98 %, respectively. In the stage of damage development, the proportions of shear cracks reached 15.08 %, 17.76 %, 18.99 %, and 19.43 %, respectively. In the stage of successive damages, the proportions of shear cracks further climbed to 22.97 %, 23.52 %, 26.65 %, and 30.62 %, respectively. It is shown that corrosion reduces shear load carrying capacity and structural stability.

In summary, the present study demonstrates several key advantages of the proposed approach: (1) non-destructive acoustic-emission monitoring obviates the need for destructive testing; (2) the Ib-value and RA–AF parameters enable real-time, scalable diagnosis of damage evolution; and (3) Gaussian clustering permits automated classification of crack events, paving the way for field deployment.

Nonetheless, certain limitations must be acknowledged: the sample size was limited, environmental variability was not addressed under laboratory conditions, and ambiguities in AE ringing and Ib-value trends likely stem from sensor configuration, signal reception geometry, and the threshold-based filtering of low-amplitude signals. Future work will expand testing to a larger cohort of beams, evaluate performance on bridge girders under realistic environmental conditions, and incorporate machine-learning techniques for enhanced noise reduction and signal processing.

CRediT authorship contribution statement

Tanbo Pan: Writing – review & editing, Methodology, Investigation, Conceptualization. **Zijun Shu:** Writing – original draft, Methodology, Investigation. **Yongcheng Liu:** Writing – review & editing, Methodology, Investigation. **Beyazit Bestami Aydin:** Supervision, Methodology, Investigation. **Yang Li:** Methodology, Investigation. **Yujue Zhou:** Methodology, Investigation. **Yubao Zhou:** Supervision.

Declaration of competing interest

The authors declare that they have no known competing financial interests or personal relationships that could have influenced the work reported in this paper.

Acknowledgments

The authors acknowledge financial support from the National Natural Science Foundation of China (No. 52468023) and the Early Career Youth Science and Technology Talent Training Program of Jiangxi Province (No. 20244BCE52161). Additionally, Yongcheng Liu and Yubao Zhou extend their gratitude for the financial assistance provided by the China Scholarship Council (CSC).

Data availability

Data will be made available on request.

References

[1] Chen Y, Zhu S, Ye SH, Ling YF, Wu D, Zhang GQ, et al. Acoustic Emission study on the damage evolution of a corroded reinforced concrete column under axial loads. Crystals 2021;11(1).
[2] Verstrynge E, Van Steen C, Vandecruys E, Wevers M. Steel corrosion damage monitoring in reinforced concrete structures with the acoustic emission technique: a review. Constr Build Mater 2022;349.

[3] Zaki A, Chai HK, Behnia A, Aggelis DG, Tan JY, Ibrahim Z. Monitoring fracture of steel corroded reinforced concrete members under flexure by acoustic emission technique. Constr Build Mater 2017;136:609–18.
[4] Van Steen C, Verstrynge E. Degradation monitoring in reinforced concrete with 3D localization of rebar corrosion and related concrete cracking. Appl Sci-Basel 2021;11(15).
[5] Abouhussien AA, Hassan AAA. Acoustic emission-based analysis of bond behavior of corroded reinforcement in existing concrete structures. Struct Control Hlth 2017;24(3).
[6] A. Deifalla, Evaluate Effect of Various Parameters on the Shear Strength of FRP-Reinforced Concrete Beams with or Without Stirrups, Proceedings of the 2nd International Civil Engineering and Architecture Conference, Ceac 2022 279 (2023) 293-303.
[7] Hamoda A, Elsamak G, Emara M, Ahmed M, Liang QQ. Experimental and numerical studies of reinforced concrete beam-to-steel column composite joints subjected to torsional moment. Eng Struct 2023;275.
[8] Lin G, Zeng JJ, Liang SD, Liao JJ, Zhuge Y. Seismic behavior of novel GFRP bar reinforced concrete beam-column joints internally reinforced with an FRP tube. Eng Struct 2022;273.
[9] Saeed YM, Aules WA, Rad FN. Flexural strengthening of RC columns with EB-CFRP sheets and NSM-CFRP rods and ropes. Compos Struct 2022;301.
[10] Sun YL, Fu JY, Sun ZY, Zhang J, Wei Y, Wu G. Flexural behavior of concrete beams reinforced by partially unbonded steel-FRP composite bars. Eng Struct 2022;272.
[11] H.H. Mhanna, R.A. Hawileh, J.A. Abdalla, Effect of FRP Anchor Inclination Angle on Shear Strengthening of Reinforced Concrete T-beams, 10th International Conference on Frp Composites in Civil Engineering (Cice 2020/2021) 198 (2022) 2169-2179.
[12] Ebead U, El Refai A, Shrestha K, Nanni A. Soffit and U-wrap fabric-reinforced cementitious matrix strengthening for reinforced concrete beams. ACI Struct J 2019;116(2):267–78.
[13] Elghazy M, El Refai A, Ebead U, Nanni A. Corrosion-damaged RC beams repaired with fabric-reinforced cementitious matrix. J Compos Constr 2018;22(5).
[14] Zheng YL, Zhou YJ, Zhou YB, Pan TB, Zhang Q, Liu D. Cracking behavior of reinforced concrete beams strengthened with CFRP anchorage system under cyclic and monotonic loading. Eng Struct 2020;207.
[15] Godat A, Hammad F, Chaallal O. State-of-the-art review of anchored FRP shear-strengthened RC beams: a study of influencing factors. Compos Struct 2020;254.
[16] Zaki MA, Rasheed HA, Alkhrdaji T. Performance of CFRP-strengthened concrete beams fastened with distributed CFRP dowel and fiber anchors. Compos Part B-Eng 2019;176.
[17] Zaki MA, Rasheed HA. Impact of efficiency and practicality of CFRP anchor installation techniques on the performance of RC beams strengthened with CFRP sheets. Can J Civil Eng 2019;46(9):796–809.
[18] Sun W, Liu SK, Zhang CY. An effective improvement for enhancing the strength and feasibility of FRP spike anchors. Compos Struct 2020;247.
[19] Mhanna HH, Hawileh RA, Abdalla JA. Shear behavior of RC T-beams externally strengthened with anchored high modulus carbon fiber-reinforced polymer (CFRP) laminates. Compos Struct 2021;272.
[20] Akhtar A, Kung D, Westbrook DR. Acoustic emission from fiber reinforced plastic damaged hoop wrapped cylinders. Mater Eval 2000;58(3):462–9.
[21] de Oliveira R, Marques AT. Health monitoring of FRP using acoustic emission and artificial neural networks. Comput Struct 2008;86(3–5):367–73.
[22] Ma G, Li H, Zhou WS, Xian GJ. Acoustic emission monitoring of concrete columns and beams strengthened with fiber reinforced polymer sheets. Proc SPIE 2012;8347.
[23] Mazlan SMSS, Abdullah SR, Shahidan S, Noor SRM. A review of the application Acoustic Emission (AE) incorporating mechanical approach to monitor Reinforced concrete (RC) strengthened with Fiber Reinforced Polymer (FRP) properties under fracture. Iop Conf Ser-Mat Sci 2017;271.
[24] Yi TY, Wang H, Xie JT, Wang WS. Flexural Strength and Acoustic damage Characteristics of Steel Bar Reactive Powder Concrete. Appl Sci-Basel 2021;11(15).
[25] Xu J, Niu XL, Yao ZY. Mechanical properties and acoustic emission data analyses of crumb rubber concrete under biaxial compression stress states. Constr Build Mater 2021;298.
[26] Brucely Y, Shaji YC, Bejaxhin ABH, Abeens M. Online acoustic emission measurement of tensile strength and wear rate for AA8011-TiC-ZrB2 hybrid composite. Surf Topogr-Metrol 2022;10(4).
[27] Han RQ, Li SL, Sun WC. Effect of grouting material strength on bond strength of sleeve and acoustic emission characterization of bond failure damage process. Constr Build Mater 2022;324.
[28] Johnson M. Waveform based clustering and classification of AE transients in composite laminates using principal component analysis. NDT and E Int 2002;35(6):367–76.
[29] Barre S, Benzeggagh ML. On the use of acoustic-emission to investigate damage mechanisms in glass-fiber-reinforced polypropylene. Compos Sci Technol 1994;52(3):369–76.
[30] Mandal DD, Bentahar M, El Mahi A, Brouste A, El Guerjouma R, Montresor S, et al. Acoustic emission monitoring of progressive damage of reinforced concrete T-beams under four-point bending. Materials 2022;15(10).
[31] Sharma G, Sharma S, Sharma SK. Non-destructive evaluation of steel and GFRP reinforced beams using AE and DIC techniques. Struct Eng Mech 2021;77(5):637–50.
[32] Ohtsu M, Watanabe H. Quantitative damage estimation of concrete by acoustic emission. Constr Build Mater 2001;15(5–6):217–24.
[33] Ohtsu M. Estimation of crack and damage development in concrete by quantitative acoustic emission analysis. Mater Eval 1999;57(5):521–5.
[34] Yun HD, Choi WC, Seo SY. Acoustic emission activities and damage evaluation of reinforced concrete beams strengthened with CFRP sheets. NDT and E Int 2010;43(7):615–28.
[35] Sagar RV, Rao MVMS. An experimental study on loading rate effect on acoustic emission based b-values related to reinforced concrete fracture. Constr Build Mater 2014;70:460–72.
[36] Ma G, Li H. Acoustic emission monitoring and damage assessment of FRP-strengthened reinforced concrete columns under cyclic loading. Constr Build Mater 2017;144:86–98.
[37] Li DS, Hai C, Ou JP. Fracture behavior and damage evaluation of polyvinyl alcohol fiber concrete using acoustic emission technique. Mater Design 2012;40:205–11.
[38] ElBatanouny MK, Ziehl PH, Larosche A, Mangual J, Matta F, Nanni A. Acoustic emission monitoring for assessment of prestressed concrete beams. Constr Build Mater 2014;58:46–53.
[39] Di Benedetti M, Nanni A. Acoustic Emission Intensity Analysis for In Situ Evaluation of Reinforced Concrete Slabs. J Mater Civil Eng 2014;26(1):6–13.
[40] Pan TB, Zheng YL, Zhou YJ, Liu YC, Yu KL, Zhou YB. Coupled effects of corrosion damage and sustained loading on the flexural behavior of RC beams strengthened with CFRP anchorage system. Compos Struct 2022;289.
[41] Zheng YL, Wen Y, Pan TB, Liu YC, Zhou YJ, Li RZ, et al. Fractal characteristics and damage evaluation of corroded beams under four-point bending tests based on acoustic emission techniques. Measurement 2022;202.
[42] Li SL, Zhang LG, Guo P, Zhang P, Wang C, Sun WC, et al. Characteristic analysis of acoustic emission monitoring parameters for crack propagation in UHPC-NC composite beam under bending test. Constr Build Mater 2021;278.
[43] Chen XD, Feng L, Wang XQ, Chen C, Diao HG. Acoustic emission characteristics of fatigue failure process of self-compacting rubberized concrete pavement slabs. Int J Pavement Eng 2022;23(12):4149–59.
[44] Zhang XC, Li B. Damage characteristics and assessment of corroded RC beam-column joint under cyclic loading based on acoustic emission monitoring. Eng Struct 2020;205.
[45] Abouhussien AA, Hassan AAA, AbdelAleem BH. Acoustic Emission Analysis of Self-Consolidating Rubberized Concrete Beam-Column Connections under Cyclic Loading. ACI Struct J 2019;116(6):41–51.
[46] (!!! INVALID CITATION !!! [47]).
[47] Chen C, Fan XQ, Chen XD. Experimental investigation of concrete fracture behavior with different loading rates based on acoustic emission. Constr Build Mater 2020;237.
[48] Liu WK, Zhou WS, Li H. Acoustic emission characteristics of Pykrete under uniaxial compression. Cold Reg Sci Technol 2022;202.
[49] N. Nor, N. Bunnori, A. Ibrahim, S. Shahidan, S. Basri, S.N.M. Saliah, B-Value Analysis of AE Signal Subjected to Stepwise Loading, Adv Mater Res-Switz 403-408 (2012) 4126-+.
[50] Sagasta F, Zitto ME, Piotrkowski R, Benavent-Climent A, Suarez E, Gallego A. Acoustic emission energy b-value for local damage evaluation in reinforced concrete structures subjected to seismic loadings. Mech Syst Signal Pr 2018;102:262–77.
[51] Xu J, Shu SR, Han QH, Liu C. Experimental research on bond behavior of reinforced recycled aggregate concrete based on the acoustic emission technique. Constr Build Mater 2018;191:1230–41.
[52] Zhang YW, Tan GJ, Wang SR, Cheng YC, Yang ST, Sun X. Flexural Characteristics Evaluation for Reinforced Concrete Affected by Steel Corrosion based on an Acoustic Emission Technique. Appl Sci-Basel 2019;9(8).